Measuring Residual Stresses by Hole-Drilling and Coherent Optics Techniques: A Numerical Calibration

F. M. Furgiuele
Research Engineer.
Mem. ASME

L. Pagnotta
Ph.D. Student.

A. Poggialini
Associate Professor.
Mem. ASME

Department of Mechanical Engineering,
University of Calabria,
87030 Cosenza, Italy

Hole-drilling is a widely accepted method for determining residual stresses from the relaxation data obtained by a strain-gage rosette. Several researchers have recently investigated the alternative of employing interferometric techniques to reveal the displacement field produced by hole-drilling. As in the case of the standardized hole-drilling strain-gage method, proper calibration constants must be assessed so that this procedure can be effectively employed. This paper reports the displacement calibration constants derived from the results of an extensive numerical analysis. The constants proposed enable a uniform residual stress field to be determined, whatever the displacement component detected. The most commonly employed coherent optics techniques have been considered; computer-generated fringe patterns are reported and criteria are suggested to derive the stress field from fringe readings taken around the edge of the hole.

1 Introduction

Hole-drilling is a widely employed technique for determining residual stresses near the surface of a material. The procedure involves measuring the change in strains or displacements produced by the hole; the quantities measured are then related to the residual stresses present in the material before drilling. The method can be considered semidestructive whenever the size of the hole is so small that the structural integrity of the part is not significantly affected.

The standard implementation of the method [1] uses strain-gages, in the form of a three-element rosette, to detect the change in radial strains. The empirical relationship, whereby the magnitudes and principal directions of the residual stresses can be derived from the strain-gage readings, differs from the theoretical Kirsch solution in that two constants must be determined by either a numerical or experimental calibration. Since these constants, which allow for both the finite gage area and finite hole depth, are material dependent, the calibration should be repeated for every particular material tested. As also suggested in the ASTM standards [1], this can be avoided by using the dimensionless and practically material independent constants obtained by Schajer from an extensive series of numerical calibrations [2]. Provided that the values of the dimensionless constants are given for the particular hole-rosette configuration, the calculation of the material-dependent calibration constants only requires the elastic properties of the material (Young's modulus E and Poisson's ratio ν) to be known. It must, however, be pointed out that errors due to imperfect hole execution can only be eliminated by an individual, experimental calibration test.

Numerical solutions obtained for blind holes of varying depths [3] have also provided calibration constants enabling the incremental drilling technique to be used for determining variation of residual stresses with depth. Results indicate that stresses can be evaluated with reasonable accuracy to a depth of about one-half the hole diameter below the surface.

During the last two decades coherent optics has provided several interferometric techniques which enable full-field surface displacements to be determined with an accuracy of approximately one-half the wavelength of light without contact with the surface investigated. While the fringe patterns observed in both moiré interferometry and speckle photography are directly related to the components in any in-plane direction (defined a priori in the first case), holographic interferometry is particularly suitable for detecting the out-of-plane displacements, although it can in fact be used to measure the displacement component along any non-in-plane direction; speckle interferometry, on the other hand, can be conveniently employed both for detecting in-plane or out-of-plane displacement components and eliminates the need for photographic processing.

The feasibility of employing interferometric techniques to measure the change in displacements occurring in the vicinity of the hole has been recently investigated [4-8]. Besides eliminating the main source of inaccuracy in the hole-drilling strain-gage method, i.e., a possible misalignment between the hole and the rosette, use of interferometric techniques enables measurement to be made at the edge of the hole, or in its proximity, where the maximum relaxation effect occurs. It must,

Contributed by the Materials Division for publication in the JOURNAL OF ENGINEERING MATERIALS AND TECHNOLOGY. Manuscript received by the Materials Division July 6, 1989; revised manuscript received May 18, 1990.

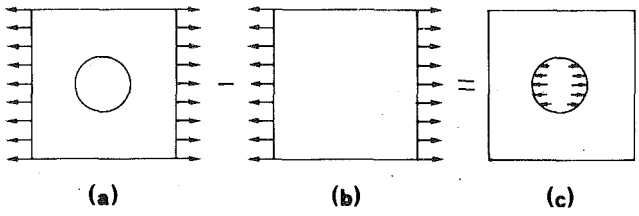

Fig. 1 Application of superposition principle

however, be pointed out that the sensitivity, defined as number of fringes over stress amplitude, cannot be considered satisfactory. In the more demanding applications it is therefore necessary either to employ experimental techniques enabling the fractional fringe order to be more accurately determined or else to carry out a numerical processing of multiple fringe readings. On the other hand, the full field representation of the displacement components can give a deeper insight into the whole stress field relieved by the removal of material. Although variations in residual stress distribution are not considered in this paper, the information carried by the whole fringe pattern around the hole might enable complex states of stress to be reconstructed.

This paper reports the results of a boundary element analysis whereby it was possible to establish an empirical relationship between a uniform state of residual stress and the in-plane and out-of-plane components of displacements at the edge of the hole. The calibration constants thus obtained allow residual stresses to be determined when the blind hole method is used in conjuction with different interferometric techniques.

2 Boundary Element Calculations

All the calculations have been carried out by the boundary element code BEE [9] for three-dimensional elasto-static analysis. Eight-node isoparametric elements have been used.

A square plate containing a center circular hole was considered in the analysis. In order to make the boundary effects negligible, the thickness and width of the plate were taken to be, respectively, 20 and 40 times the hole diameter D. Because of symmetry only one-fourth of the plate was considered.

The plate was assumed to be subjected to a uniform uniaxial tensile stress σ. In order to derive directly the displacement perturbation produced by hole-drilling, the loading was applied to the boundary of the hole as shown in Fig. 1(*c*). Since a linear elastic material was considered in the analysis, the superposition principle applies as illustrated in the same Fig. 1 where the loading conditions represented in (*a*) and (*b*), respectively, correspond to the stress distribution which is present in the plate after and before the hole has been drilled.

3 Residual-Stress/Displacement Relations for a Through Hole

When assessing the hole-drilling strain-gage method, it is commonly assumed that the classical theoretical plane stress solution for an infinite plate with a circular hole can closely approximate the distribution of the radial strain components on the surface of a thick plate containing a through hole and hence that a proper analysis is only needed to account for a blind-hole situation. The present numerical investigation has been carried out to investigate whether this idealization can be extended to the tangential components of strain and displacement which can as well be of interest when using an interferometric technique. The analysis is also aimed at deriving an empirical relationship for the distribution of the out-of-plane displacement, which obviously cannot be derived from a two-dimensional solution.

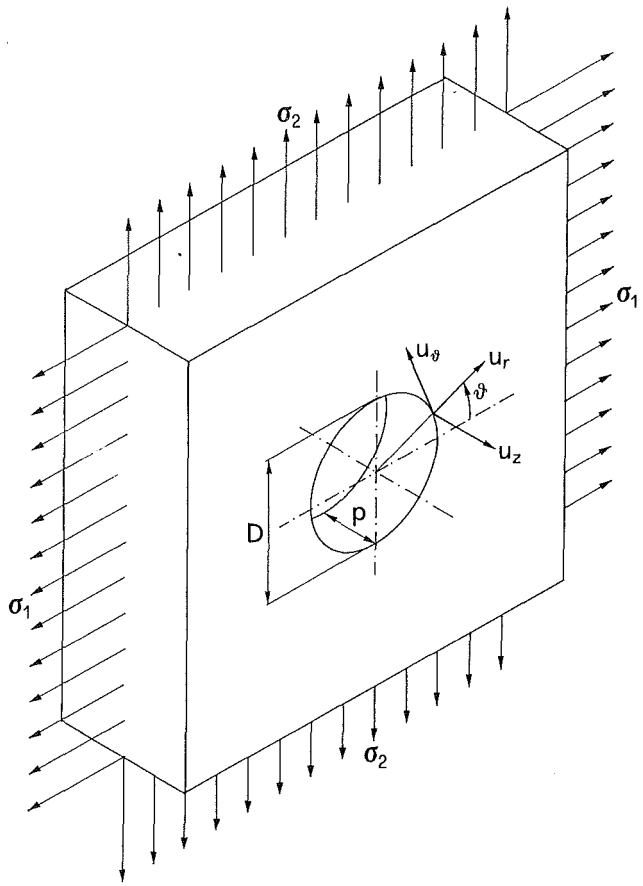

Fig. 2 Displacement components at the edge of a hole produced in a uniformly stressed body

Referring to Fig. 2, the theoretical solution for the radial and tangential components of displacement, u_r and u_θ, respectively, on the border of a circular hole produced in a thin infinite plate under a biaxial state of stress (σ_1, σ_2)

$$\bar{\bar{u}}_r = D\left(\frac{1+\nu}{4}\frac{\sigma_1+\sigma_2}{E} + \frac{3-\nu}{4}\frac{\sigma_1-\sigma_2}{E}\cos 2\theta\right)$$
$$\bar{\bar{u}}_\theta = D\left(-\frac{3-\nu}{4}\frac{\sigma_1-\sigma_2}{E}\sin 2\theta\right) \tag{1}$$

can be straightforwardly derived by subtracting the solution for the plate without the hole from the well-known Kirsch solution (cfr., Fig. 1). When the actual three-dimensional problem is considered the in-plane components exhibit the same dependence on the angle θ

$$\bar{u}_r = D\left(\bar{A}_r\frac{\sigma_1+\sigma_2}{E} + \bar{B}_r\frac{\sigma_1-\sigma_2}{E}\cos 2\theta\right)$$
$$\bar{u}_\theta = D\left(-\bar{B}_\theta\frac{\sigma_1-\sigma_2}{E}\sin 2\theta\right) \tag{2}$$

while the out-of-plane displacement u_z can be expressed as

$$\bar{u}_z = D\left(\bar{A}_z\frac{\sigma_1+\sigma_2}{E} + \bar{B}_z\frac{\sigma_1-\sigma_2}{E}\cos 2\theta\right) \tag{3}$$

where coefficients $\bar{A}_r$, $\bar{B}_r$, $\bar{B}_\theta$, $\bar{A}_z$, and $\bar{B}_z$ depend on the material constants only.

Since the plane stress solution is the exact three-dimensional solution when a planar hydrostatic state of stress $(\sigma_1 = \sigma_2)$ is assumed, it follows that:

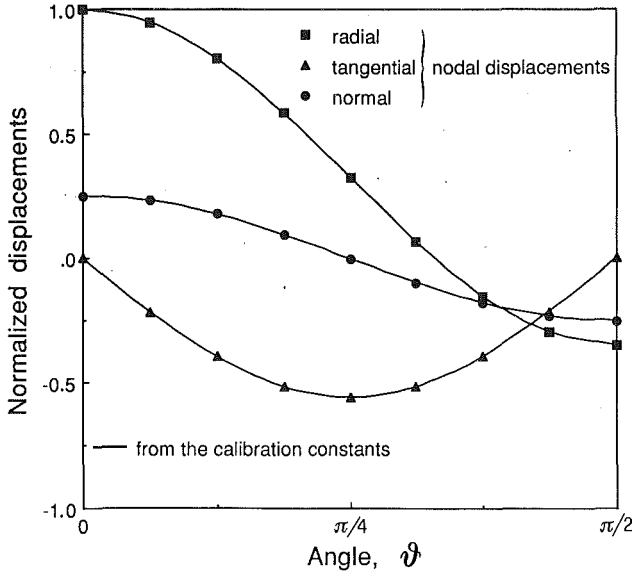

Fig. 3 Variation of the cylindrical components of displacement along the edge of a through hole produced in a uniaxially stressed body

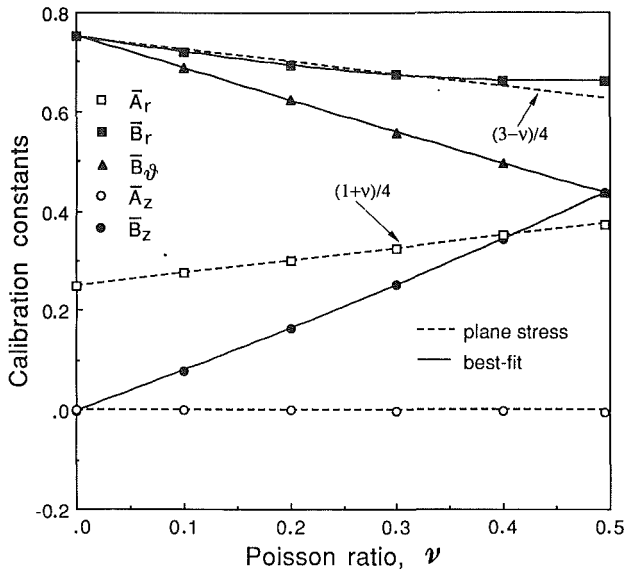

Fig. 4 Variation of the displacement calibration constants with Poisson's ratio for a through hole

$$\bar{A}_r = \frac{1+\nu}{4} \tag{4a}$$

$$\bar{A}_z = 0 \tag{4b}$$

Relation (4*b*) derives from the consideration that the axial component of the relieved strain resulting from the plane stress solution is null when a hydrostatic state of stress is present (i.e., when the hole in Fig. 1(*c*) is subjected to a uniform internal pressure).

In order to compare the theoretical displacement distribution with the numerical three-dimensional solution and to derive an empirical relationship between the various coefficients and Poisson's ratio, the analysis has been carried out for values of ν ranging from 0.0 to 0.495. The value of 0.5 was avoided in the computation because of the larger numerical error.

Denoting by $\bar{U}_r$, $\bar{U}_\theta$, and $\bar{U}_z$ the nondimensional components of displacement computed for the case of uniaxial state of stress ($\sigma_1 = \sigma$, $\sigma_2 = 0$):

$$\bar{U}_r(\theta) = \frac{\bar{u}_r(\theta)}{D} \Big/ \frac{\sigma}{\mathrm{E}}$$

$$\bar{U}_\theta(\theta) = \frac{\bar{u}_\theta(\theta)}{D} \Big/ \frac{\sigma}{\mathrm{E}} \tag{5}$$

$$\bar{U}_z(\theta) = \frac{\bar{u}_z(\theta)}{D} \Big/ \frac{\sigma}{\mathrm{E}}$$

the five coefficients can be calculated as:

$$\bar{A}_r = \frac{\bar{U}_r(\theta=0) + \bar{U}_r(\theta=\pi/2)}{2} \qquad \bar{B}_r = \frac{\bar{U}_r(\theta=0) - \bar{U}_r(\theta=\pi/2)}{2}$$

$$\bar{B}_\theta = -\bar{U}_\theta(\theta=\pi/4) \tag{6}$$

$$\bar{A}_z = \frac{\bar{U}_z(\theta=0) + \bar{U}_z(\theta=\pi/2)}{2} \qquad \bar{B}_z = \frac{\bar{U}_z(\theta=0) - \bar{U}_z(\theta=\pi/2)}{2}$$

Within the whole range of ν, an excellent agreement was found between the numerical values of $\bar{A}_r$ (percentage error within 0.69), $\bar{A}_z$ (highest absolute value lower than $0.5 \cdot 10^{-2}$), and their exact values given in (4), thus confirming the accuracy of the numerical solution. The coefficients could of course be derived from the whole set of nodal displacement along the edge of the hole by a best-fit procedure. This was, however, considered unnecessary because of the exceedingly close agreement (within 0.5 percent) between the displacement values computed using (2) and (3) and those obtained at the nodal points by boundary element analysis (see Fig. 3 for the case $\nu = 0.3$).

Figure 4 plots the values calculated for coefficients $\bar{A}_r$, $\bar{B}_r$, $\bar{B}_\theta$, $\bar{A}_z$, $\bar{B}_z$ versus Poisson's ratio together with the corresponding plane stress values (where defined). A comparison between the two sets of values indicates that the two-dimensional solution can only be considered acceptable for coefficient $\bar{B}_r$. Where $\bar{B}_\theta$ is concerned, significant discrepancies are in fact to be observed, the greatest deviations occurring for the highest values of ν. The values numerically calculated for $\bar{B}_\theta$ appear, nevertheless, to be still linearly dependent on the value of Poisson's ratio. By applying a least-square minimization-error procedure the following empirical relationship was derived

$$\bar{B}_\theta(\nu) = 3/4 - 0.636\nu \tag{7}$$

which accurately fits (within 0.31 percent) the $\bar{B}_\theta$ values calculated over the whole range of ν. Note that, both in this and the following calculations carried out by the best-fit procedure, the value of the coefficient at $\nu = 0$ was derived from the exact plane stress solution.

When the same procedure was applied to coefficient $\bar{B}_r$, the quadratic relationship

$$\bar{B}_r(\nu) = 3/4 - 0.365\nu + 0.348\nu^2 \tag{8}$$

was found to predict the numerical values with a 0.33 percent accuracy. When the above relation is compared with that derived from the plane stress solution, it can be observed that the difference which accounts for the three-dimensional effect

$$\bar{B}_r(\nu) - \frac{3-\nu}{4} = 0.115\nu + 0.348\nu^2 \tag{9}$$

is lower than 5.22 percent in the whole range and null for a value of ν slightly above 0.3, thus further validating the assumption commonly made in assessing the hole-drilling strain-gage method.

When the best-fit procedure was employed to derive coeffi-

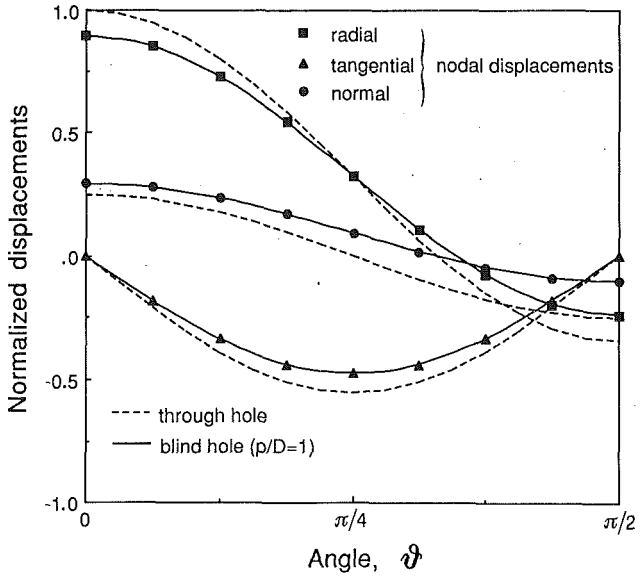

Fig. 5 Variation of cylindrical components of displacement along the edge of a blind hole ($p/D = 1$) produced in a uniaxially stressed body

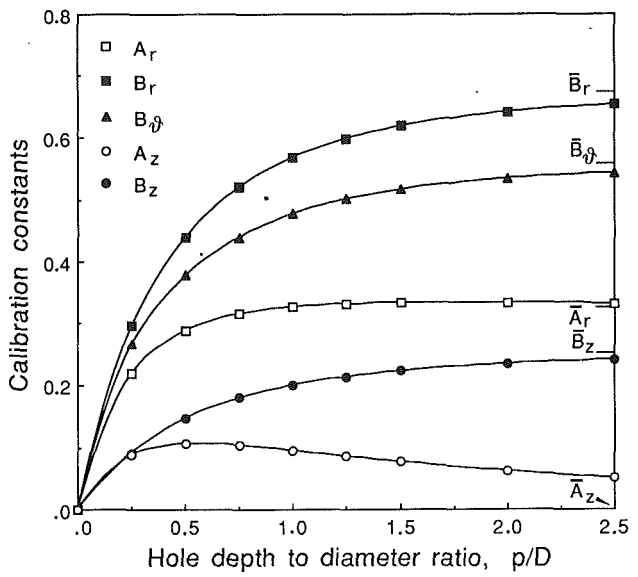

Fig. 6 Variation of the displacement calibration constants with the ratio hole depth/hole diameter for a blind hole ($\nu = 0.3$)

cient $\bar{B}_z$ as a function of ν, a quadratic relationship was again obtained

$$\bar{B}_z(\nu) = 0.770\nu + 0.221\nu^2 \tag{10}$$

The difference between the values obtained for $\bar{B}_z$ from the results of the boundary element analysis and those calculated by relation (10) was within 0.31 percent.

By substituting the expressions given above for the coefficients appearing in equations (2) and (3), it is possible to predict the displacement distribution along the boundary of a through hole for any particular value of ν.

It must however be pointed out that the empirical relationships previously proposed for coefficients $\bar{B}_r$, $\bar{B}_\theta$, and $\bar{B}_z$ can only be considered valid when the ratio of plate thickness to hole diameter is sufficiently high to establish a plane strain condition in the center layer of the plate. For lower ratios the displacement distribution is in fact dependent on the thickness to diameter ratio.

4 Residual-Stress/Displacement Relations for a Blind Hole

In order to derive calibration constants to be used in the hole-drilling technique, the analysis has been carried out for hole depths p ranging from 0.25 to 2.5 times the hole diameter D. The ratios of both plate width and plate thickness to hole diameter were the same as those assumed in the case of the through hole previously analyzed.

The nondimensional nodal values of displacements U_r, U_θ, and U_z, calculated for the case of uniaxial state of stress, $\nu = 0.3$ and $p/D = 1.0$, are plotted in Fig. 5 versus the angle θ. The same figure also reports the displacements $\bar{U}_r$, $\bar{U}_\theta$, and $\bar{U}_z$ previously obtained for the through hole and the same value of Poisson's ratio.

As to be expected, a comparison between the two sets of values clearly indicates that the three displacement components, although they obviously exhibit the same θ-dependence, differ significantly from the through hole components; in particular a constant term is now present in the expression for the normal component of displacement.

Substituting the blind hole coefficients (A and B) for the through hole coefficients ($\bar{A}$ and $\bar{B}$) in relations (1) and (2), the displacement variation along the edge of a blind hole can be given as:

Table 1 Numerical values of displacement calibration constants for $\nu = 0.3$

p/D	A_r	B_r	B_θ	A_z	B_z
0.25	0.2197	0.2961	0.2666	0.08788	0.09116
0.50	0.2890	0.4396	0.3775	0.1057	0.1471
0.75	0.3160	0.5198	0.4397	0.1030	0.1797
1.00	0.3270	0.5678	0.4771	0.09479	0.2001
1.25	0.3315	0.5982	0.5006	0.08561	0.2137
1.50	0.3331	0.6183	0.5161	0.07696	0.2231
2.00	0.3332	0.6415	0.5337	0.06242	0.2346
2.50	0.3319	0.6533	0.5426	0.05122	0.2408

$$u_r = D\left(A_r\frac{\sigma_1+\sigma_2}{E} + B_r\frac{\sigma_1-\sigma_2}{E}\cos 2\theta\right)$$

$$u_\theta = D\left(-B_\theta\frac{\sigma_1-\sigma_2}{E}\sin 2\theta\right) \tag{11}$$

$$u_z = D\left(A_z\frac{\sigma_1+\sigma_2}{E} + B_z\frac{\sigma_1-\sigma_2}{E}\cos 2\theta\right)$$

The coefficients, which in this case depend not only on Poisson's ratio but also on p/D, can be calculated from nodal displacements by relations (6) with $U(\theta)$ replacing $\bar{U}(\theta)$.

The values of the five coefficients obtained for a Poisson's ratio of 0.3 are plotted versus the p/D ratio in Fig. 6. The same figure also shows the asymptotic values ($p/D = \infty$), which can either be derived from the graph in Fig. 4 or calculated by the analytical expressions given in the previous paragraph. In order that relations (11) be more effectively employed the numerical values of the coefficients calculated are reported in Table 1.

As to be expected, the blind hole coefficients introduced above depend significantly on the material constant ν. In order to eliminate the need to repeat the calibration whenever the value of Poisson's ratio of the material tested differs from 0.3,

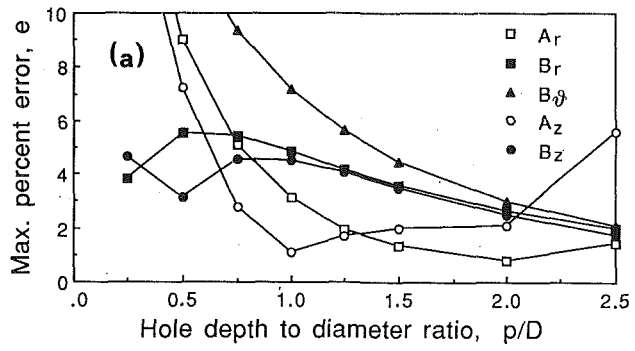

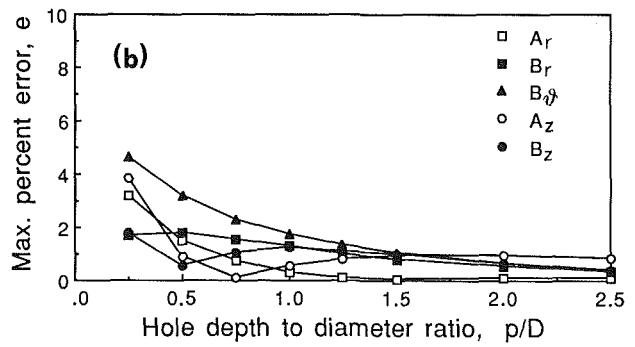

Fig. 7 Plots of the maximum percentage errors in the values of calibration constants obtained by relations (12) versus *p/D* ratio: (*a*) in the range $0.2 \le \nu \le 0.495$; (*b*) in the range $0.25 \le \nu \le 0.35$

a similar approach was attempted to that proposed by Schajer [2] and reported in the ASTM standard for the radial strain coefficients used in the hole-drilling strain-gage method. The approach is based on the assumption that the blind hole coefficients exhibit the same dependence on ν as the through hole coefficients, whatever the value of p/D. Although this assumption is obviously only correct for $p/D=\infty$, it does, however, permit to calculate approximate values of the blind hole coefficients for any value of ν:

$$
\begin{aligned}
A_r'(\nu,p/D) &= A_r(\nu_0,p/D)\bar{A}_r(\nu)/\bar{A}_r(\nu_0)\\
B_r'(\nu,p/D) &= B_r(\nu_0,p/D)\bar{B}_r(\nu)/\bar{B}_r(\nu_0)\\
B_\theta'(\nu,p/D) &= B_\theta(\nu_0,p/D)\bar{B}_\theta(\nu)/\bar{B}_\theta(\nu_0) \qquad (12)\\
A_z'(\nu,p/D) &= A_z(\nu_0,p/D)A_z(\nu,p/D=1)/A_z(\nu_0,p/D=1)\\
B_z'(\nu,p/D) &= B_z(\nu_0,p/D)\bar{B}_z(\nu)/\bar{B}_z(\nu_0)
\end{aligned}
$$

The analytical relations given in the previous paragraph can be employed to calculate $\bar{A}_r$, $\bar{B}_r$, $\bar{B}_\theta$, and $\bar{B}_z$ whereas, taking ν_0 to be 0.3, the values of A_r, B_r, B_θ, A_z, B_z can be found in Table 1.

Since the constant term in the expression for normal displacement variation around a through hole is equal to zero (see previous paragraph), the normalization factor for coefficient A_z cannot be defined as $\bar{A}_z(\nu)/\bar{A}_z(\nu_0)$. An alternative factor $A_z(\nu,p/D=1)/A_z(\nu_0,p/D=1)$ is proposed where $A_z(\nu,p/D=1)$ is given by the analytical relationship:

$$A_z(\nu,p/D=1)=0.071+0.089\nu-0.036\nu^2 \qquad (13)$$

which has been derived by applying a best-fit procedure to the numerical results obtained from analyses carried out for $p/D=1$ and values of ν ranging from 0.0 to 0.495.

Unfortunately ratios $A_r/\bar{A}_r$, $B_r/\bar{B}_r$, etc., far from being functions of p/D only, still exhibit a significant dependence on ν. As a consequence, relations (12) can only be employed to estimate the blind hole coefficients for values of ν in a small range around 0.3 or for high values of p/D ratio (cf. Figs. 7(*a*) and 7(*b*) which show the percentage differences between the values of the coefficients obtained from the approximate relations (12) and those derived from a proper numerical analysis). Figure 7(*a*) plots the largest percentage difference observed in the range $0.2 \le \nu \le 0.495$ versus p/D ratio ($0.25 \le p/D \le 2.50$). The significantly lower percentage values plotted in Fig. 7(*b*) represent the maximum error encountered in the smaller range $0.25 \le \nu \le 0.35$. As to be expected the errors in A_r, B_r, B_θ, and B_z decrease as p/D increases, whereas, because of the normalization factor assumed, the error in A_z is minimum for $p/D \simeq 1$. By further reducing the range of ν to 0.28-0.33, i.e., to the range wherein the calibration constants given by Schajer for the blind hole strain-gage method can be considered material independent, the error keeps below 2 percent for $p/D \ge 0.5$ and below 1 percent for $p/D \ge 1$.

Table 2 Correction factors for deriving displacement calibration constants from the values given in Table 1 for Poisson's ratios different from 0.3

p/D	A_r^*	B_r^*	B_θ^*	A_z^*	B_z^*
0.25	0.0390	0.0200	−0.0590	0.0170	0.3029
0.50	0.1420	0.0470	−0.1900	0.0580	0.5440
0.75	0.2010	0.0350	−0.2970	0.0742	0.6840
1.00	0.2330	0.0090	−0.3770	0.0768	0.7660
1.25	0.2490	−0.0190	−0.4380	0.0735	0.8140
1.50	0.2570	−0.0430	−0.4820	0.0679	0.8440
2.00	0.2620	−0.0810	−0.5410	0.0553	0.8730
2.50	0.2620	−0.1070	−0.5760	0.0440	0.8850

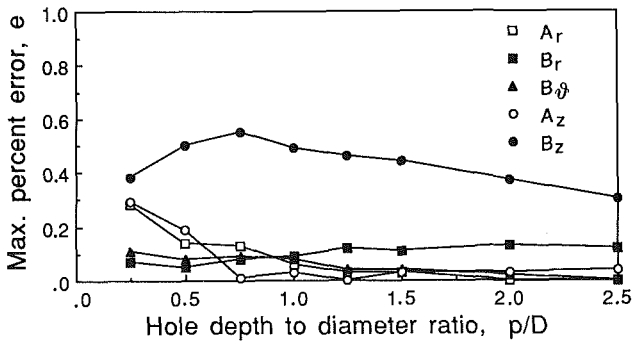

Fig. 8 Plots of the maximum percentage errors in the values of calibration constants obtained by relations (14) versus *p/D* ratio, in the range $0.25 \le \nu \le 0.35$

Although the approximate relations given above can be employed to predict with rather good accuracy the coefficient values within a small range of ν, the approach cannot be considered completely successful. A different and somewhat simpler approach is therefore proposed which enables calibration constants to be computed with considerably higher accuracy in a range of ν (say, $0.25 \le \nu \le 0.35$) which includes the values of Poisson's ratio for most metallic materials. In such a range, in fact, the variation with ν of the blind hole coefficients numerically calculated appears almost linear. By retaining only the linear term in the power series by which coefficients A_r, B_r, etc, can be expressed, approximate values for the same coefficients can be obtained as

$$
\begin{aligned}
A_r'(\nu,p/D) &= A_r(\nu_0,p/D)+A_r^*(\nu_0,p/D)(\nu-\nu_0)\\
&\cdots\cdots\cdots\cdots\cdots\cdots\cdots\cdots \qquad (14)\\
B_z'(\nu,p/D) &= B_z(\nu_0,p/D)+B_z^*(\nu_0,p/D)(\nu-\nu_0)
\end{aligned}
$$

where the values for A_r, B_r, etc ($\nu_0=0.3$) are given in Table 1.

The terms A_r^*, B_r^*, etc, which are reported in Table 2, have been computed from the respective coefficients A_r, B_r, etc, derived from the numerical analyses carried out for $\nu_1 = \nu_0 - \Delta\nu = 0.25$ and $\nu_2 = \nu_0 + \Delta\nu = 0.35$, as

$$A_r^*(\nu_0, p/D) = [A_r(\nu_2, p/D) - A_r(\nu_1, p/D)]/2\Delta\nu$$
$$\cdots\cdots\cdots\cdots\cdots\cdots\cdots\cdots \quad (15)$$
$$B_z^*(\nu_0, p/D) = [B_z(\nu_2, p/D) - B_z(\nu_1, p/D)]/2\Delta\nu$$

Figure 8 shows the maximum absolute values of the percentage differences between the coefficients derived from numerical analysis and those obtained from relations (14). A comparison between the percentage errors plotted in Fig. 8 and those given in Fig. 7(*b*) for the same range of ν, clearly confirms that a noticeably higher accuracy can be achieved by this latter approach.

5 Determining Residual Stresses

5.1 Measuring Displacements by Coherent Optics Techniques. The coherent optics techniques which are currently used in experimental stress analysis enable one or more fringe patterns to be displayed over the full field investigated, with each pattern depicting the contours of a specific displacement component.

Without entering into the details of any particular technique, the equation for predicting, and hence interpreting, fringe generation can be quite generally written as:

$$n(P) = N\frac{\mathbf{k}\cdot\mathbf{u}(P)}{\lambda} \quad (16)$$

Except for factor N, the fringe order n at point P (maximum fringe brightness for integer values: $n = 0, \pm 1, \pm 2, \ldots$) is given by the projection, along the direction defined by the unit vector $\mathbf{k} = \{k_x, k_y, k_z\}$, of the vectorial displacement $\mathbf{u}$, at the same point P, divided by the wavelength λ of the coherent radiation.

The sensitivity factor N is determined by the governing angles adopted in the optical setup. N can usually reach the optimal value of 2 fringes per wavelength, i.e., the increment between two adjacent fringes can be made as small as one half the wavelength of the coherent light source employed.

The direction of the unit vector $\mathbf{k}$ is also defined by the optical setup; each technique does however possess quite distinctive features which make it more suitable for detecting specific displacement components (holographic interferometry, normal, or quasi normal, displacements; moiré interferometry, in-plane displacements, etc.). If the surface investigated is planar and the direction of vector $\mathbf{k}$ does not significantly vary over the whole area of interest (that is, it does not depend on the position of point P), the interpretation of the fringe pattern is quite straightforward, since each fringe represents the locus of points of equal displacement in the $\mathbf{k}$ direction.

When coherent optics techniques are employed to detect the displacements produced by hole-drilling in a stressed body, whichever displacement component is observed, it is possible to deduce the state of stress from the fringe pattern, provided appropriate calibration constants are available. The five coefficients appearing in relations (11) can be employed as calibration constants in determining residual stresses by carrying out fringe readings at the edge of the hole; as will be shown later, the magnitude and orientation of the principal stresses can be derived from the fractional fringe order estimated at three points, or even two in some particular cases.

The following illustrates some procedures which can be employed to derive the state of stress from the displacements measured along the edge of the hole. Different approaches can be followed depending on the particular displacement component displayed by the fringe pattern.

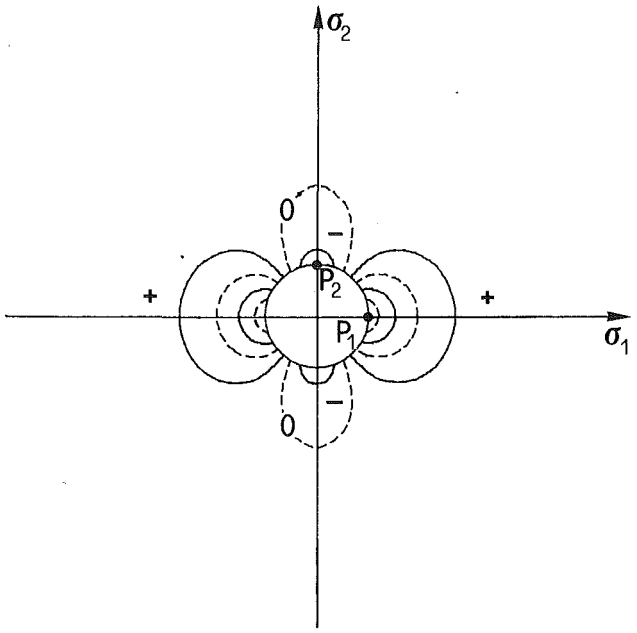

Fig. 9 Normal displacement

5.2 Determining Residual Stresses From Normal Displacements. Let us first analyze the case when normal components are detected (e.g., by holographic interferometry); relation (16) simplifies in this case to:

$$n(P) = N\frac{u_z(P)}{\lambda} \quad (17)$$

since $\mathbf{k} = \{0,0,1\}$.

Figure 9 reports a computer-generated fringe pattern which depicts the normal displacements occurring around a blind hole produced in a uniaxially stressed body ($\sigma_1 = \sigma$, $\sigma_2 = 0$). Dotted lines represent maximum fringe brightness ($n = 0, \pm 1, \pm 2, \ldots$) while continuous lines represent dark fringes ($n = \pm 0.5, \pm 1.5, \pm 2.5, \ldots$). The zero order fringe and the sign of the displacements are also indicated.

This plot, like the ones to be shown later, has been derived from the nodal displacements obtained by boundary element analysis of a blind hole with a depth to diameter ratio $p/D = 1$ and a Poisson's ratio $\nu = 0.3$; fringe spacing is consistent with $N(\sigma/E)(D/\lambda) = 8$. The above conditions could, for example, correspond to a case where:

elastic properties of the material: E = 206 GPa, $\nu = 0.3$;

state of stress: $\sigma_1 = 206$ MPa, $\sigma_2 = 0$;

drilled hole: $D = 2$ mm, $p/D = 1$;

displacement sensitivity: $N/\lambda = 4$ fringes/μm.

The principal directions are clearly indicated by the symmetry of the fringe pattern; the direction of the higher principal stress coincides with that of the diameter which intersects the edge at the points where the largest algebraic displacement occurs. It could be shown easily that the above considerations can be fully extended to the more general case of a biaxial state of stress. Two independent fringe readings at the edge of the hole are then sufficient to determine the values of the principal stresses. By substituting the last of relations (11) into (17), the fringe order variation along the border can in fact be given as:

$$n_z(\theta) = N\frac{D}{\lambda}\left(A_z\frac{\sigma_1+\sigma_2}{E} + B_z\frac{\sigma_1-\sigma_2}{E}\cos 2\theta\right) \quad (18)$$

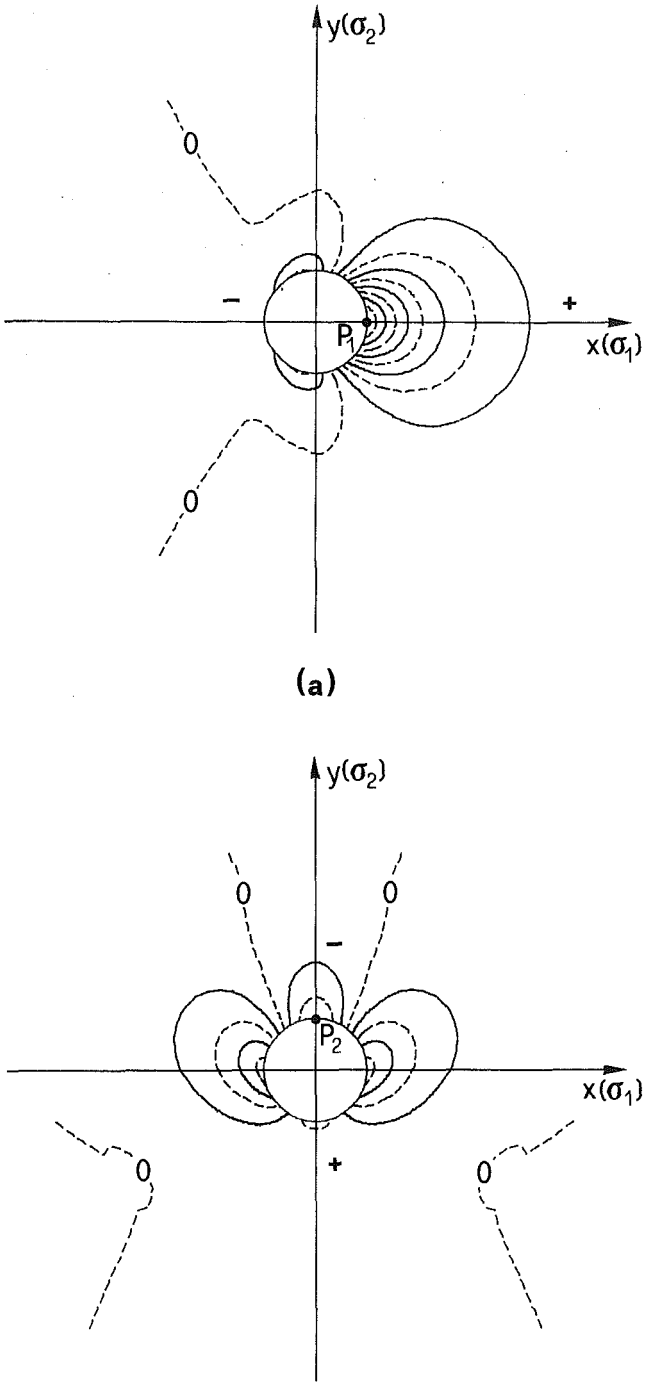

Fig. 10 Oblique displacement: (*a*) in the *xz* plane; (*b*) in the *yz* plane

When, in particular, the measurements are taken at the two points where the fringe order is respectively maximum and minimum (P_1 and P_2 in Fig. 9), the following two equations are obtained:

$$n(P_1)=n_z(0)=N\frac{D}{\lambda}\left(A_z\frac{\sigma_1+\sigma_2}{\mathrm{E}}+B_z\frac{\sigma_1-\sigma_2}{\mathrm{E}}\right)$$
$$n(P_2)=n_z\left(\frac{\pi}{2}\right)=N\frac{D}{\lambda}\left(A_z\frac{\sigma_1+\sigma_2}{\mathrm{E}}-B_z\frac{\sigma_1-\sigma_2}{\mathrm{E}}\right) \tag{19}$$

which, solved for $(\sigma_1+\sigma_2)$ and $(\sigma_1-\sigma_2)$, lead to:

$$\sigma_1+\sigma_2=\mathrm{E}\frac{\lambda}{D}\frac{n(P_1)+n(P_2)}{N(2A_z)}$$
$$\sigma_1-\sigma_2=\mathrm{E}\frac{\lambda}{D}\frac{n(P_1)-n(P_2)}{N(2B_z)} \tag{20}$$

Under the testing conditions given above, the ratio $(\sigma_1+\sigma_2)/[n(P_1)+n(P_2)]$, which is an indication of the sensitivity to the sum of the principal stresses, is equal to 135.83 MPa/fringe, whereas the ratio $(\sigma_1-\sigma_2)/[n(P_1)-n(P_2)]$, related to the sensitivity to the difference between the principal stresses, is equal to 64.34 MPa/fringe.

It is worth pointing out that, in the case of a blind hole only, it is possible to determine both the sum and difference of the stresses, and hence to separate the stress components; the coefficient A_z is in fact equal to zero for a through hole and, consequently, $n(P_2)=-n(\mathrm{P}_1)$. Where the depth of the blind hole is concerned, note that the plot given in Fig. 6 indicates that the maximum sensitivity to $(\sigma_1+\sigma_2)$ is achieved when the hole depth is about one half of the diameter. On the other hand, the maximum sensitivity to $(\sigma_1-\sigma_2)$ is reached for a through hole.

An experimental verification of the procedure given above can be found in [8].

5.3 Determining Residual Stresses from Oblique Displacements. Although the procedures previously described for deriving the stress field from the normal displacements are particularly straightforward, it must be considered that normal displacements, being essentially due to Poisson's effect, are considerably lower than in-plane displacements; by measuring the latter a higher accuracy can thus generally be achieved.

By using holographic interferometry, it is possible to reveal in-plane displacements by simply changing the viewpoint of the observer. When two displacements are detected which lie on two principal planes, the fringe order variation along the edge of the hole can be, respectively, written as:

$$n_{zx}(\theta)=N\frac{k_xu_x(\theta)+k_zu_z(\theta)}{\lambda}$$
$$n_{zy}(\theta)=N\frac{k_yu_y(\theta)+k_zu_z(\theta)}{\lambda} \tag{21}$$

where the in-plane components, u_x and u_y, of the displacements observed can be expressed as:

$$u_x(\theta)=u_r(\theta)\cos\theta-u_\theta(\theta)\sin\theta$$
$$u_y(\theta)=u_r(\theta)\sin\theta+u_\theta(\theta)\cos\theta \tag{22}$$

The corresponding fringe patterns are reported in Fig. 10(*a*) and Fig. 10(*b*), respectively, for the testing conditions given above and for values for both k_x/k_z and k_y/k_z equal to 1/3.

The fringe orders at point P_1 in Fig. 10(*a*) and at point P_2 in Fig. 10(*b*) are now given by:

$$n(P_1)=n_{zx}(0)=N\frac{D}{\lambda}\left[(k_xA_r+k_zA_z)\frac{\sigma_1+\sigma_2}{\mathrm{E}}+(k_xB_r+k_zB_z)\frac{\sigma_1-\sigma_2}{\mathrm{E}}\right]$$
$$n(P_2)=n_{zy}\left(\frac{\pi}{2}\right)=N\frac{D}{\lambda}\left[(k_yA_r+k_zA_z)\frac{\sigma_1+\sigma_2}{\mathrm{E}}-(k_yB_r+k_zB_z)\frac{\sigma_1-\sigma_2}{\mathrm{E}}\right] \tag{23}$$

By solving the above two equations, for $(\sigma_1+\sigma_2)$ and $(\sigma_1-\sigma_2)$, we obtain:

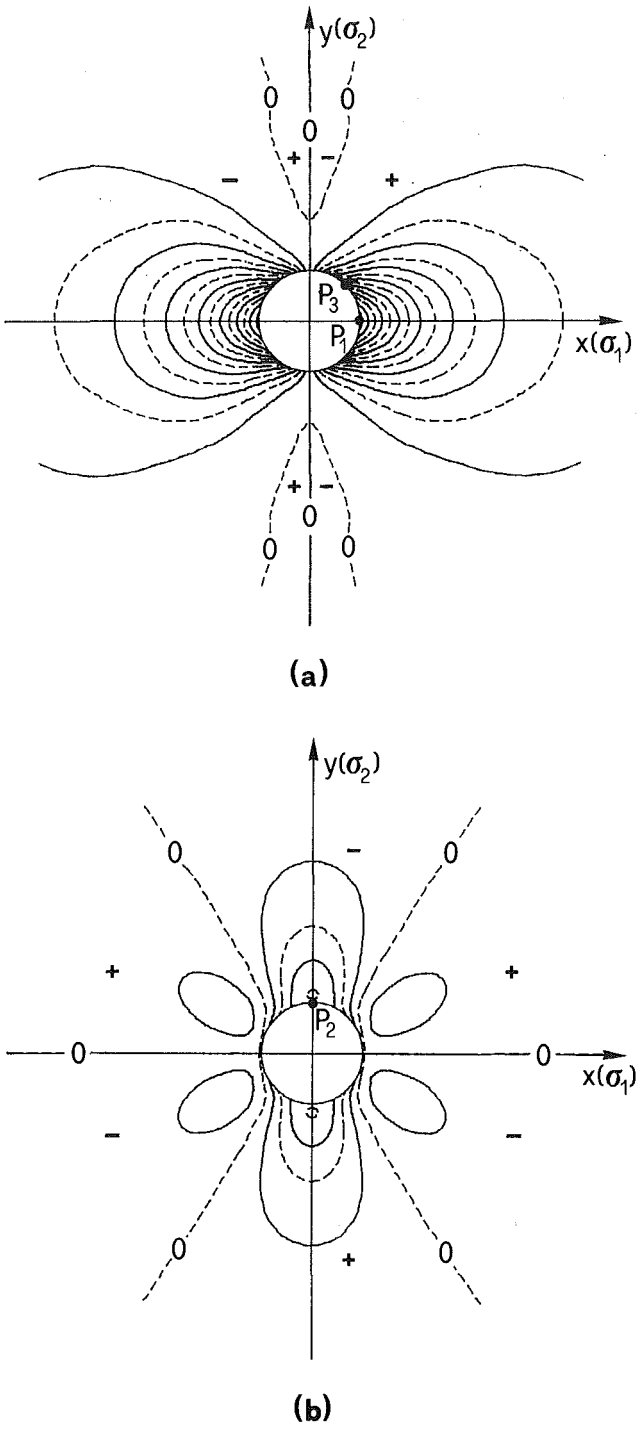

Fig. 11 In-plane displacement: (*a*) in the *x* direction; (*b*) in the *y* direction

$$\sigma_1+\sigma_2=\mathrm{E}\frac{\lambda}{D}\frac{n(P_1)+n(P_2)}{N[(k_x+k_y)A_r+2k_zA_z]}$$
$$\sigma_1-\sigma_2=\mathrm{E}\frac{\lambda}{D}\frac{n(P_1)-n(P_2)}{N[(k_x+k_y)B_r+2k_zB_z]} \tag{24}$$

For the case exemplified in Fig. 10, the ratio $(\sigma_1+\sigma_2)/[n(P_1)+n(P_2)]$ is equal to 66.60 MPa/fringe while the ratio $(\sigma_1-\sigma_2)/[n(P_1)-n(P_2)]$ is 34.86 MPa/fringe.

5.4 Determining Residual Stresses from In-Plane Displacements. Accuracy in determining the values of stress components can be further improved by employing a technique which enables the in-plane displacement components to be directly observed. In this case the fringe variation along the edge of the hole can be simply written as:

$$n_x(\theta)=N\frac{u_x(\theta)}{\lambda}$$
$$n_y(\theta)=N\frac{u_y(\theta)}{\lambda} \tag{25}$$

where the coordinate axes still define the directions of the displacements detected.

Figures 11(*a*) and 11(*b*) illustrate the fringe patterns which, respectively, depict the u_x and u_y in-plane displacement components. In this case the *x*- and *y*-directions coincide with the principal axes as is clearly indicated by the symmetry of both the patterns and by the presence of a zero-order fringe at the edge points lying on the *y*-axis in Fig. 11(*a*) and on the *x*-axis in Fig. 11(*b*).

The fringe orders at point P_1 in Fig. 11(*a*) and P_2 in Fig. 11(*b*) can be expressed in terms of the principal stresses as:

$$n(P_1)=n_x(0)=N\frac{D}{\lambda}\left(A_r\frac{\sigma_1+\sigma_2}{\mathrm{E}}+B_r\frac{\sigma_1-\sigma_2}{\mathrm{E}}\right)$$
$$n(\mathrm{P}_2)=n_y\left(\frac{\pi}{2}\right)=N\frac{D}{\lambda}\left(A_r\frac{\sigma_1+\sigma_2}{\mathrm{E}}-B_r\frac{\sigma_1-\sigma_2}{\mathrm{E}}\right) \tag{26}$$

which solved for $(\sigma_1+\sigma_2)$ and $(\sigma_1-\sigma_2)$ lead to:

$$\sigma_1+\sigma_2=\mathrm{E}\frac{\lambda}{D}\frac{n(P_1)+n(P_2)}{N(2A_r)}$$
$$\sigma_1-\sigma_2=\mathrm{E}\frac{\lambda}{D}\frac{n(P_1)-n(P_2)}{N(2B_r)} \tag{27}$$

It can be noticed that equations (27) are exactly equivalent to equations (20) where radial displacement (and related calibration constants) substitute for normal displacement.

When the same testing conditions are assumed to hold, the ratio $(\sigma_1+\sigma_2)/[n(P_1)+n(P_2)]$ is now 39.37 MPa/fringe whereas the ratio $(\sigma_1-\sigma_2)/[n(P_1)-n(P_2)]$ is 22.68 MPa/fringe, confirming the expected improvement in sensitivity.

An alternative procedure can be adopted which only requires a single fringe pattern. A second independent fringe measurement can in fact be taken on the same pattern. Assuming the second reading to be at 45 deg, the fringe orders at points P_3 in Fig. 11(*a*) is given by:

$$n(P_3)=n_x\left(\frac{\pi}{4}\right)=N\frac{D}{\lambda}\frac{\sqrt{2}}{2}\left(A_r\frac{\sigma_1+\sigma_2}{\mathrm{E}}+B_\theta\frac{\sigma_1-\sigma_2}{\mathrm{E}}\right) \tag{28}$$

The values of the principal stresses can thus be determined by solving for $(\sigma_1+\sigma_2)$ and $(\sigma_1-\sigma_2)$ equation (28) together with the first of (26); because of the relatively small difference between B_r and B_θ, the accuracy is however lower than that yielded by using relations (27).

Whatever the procedure adopted, it must be pointed out that the possibility of detecting the components of displacement along particular directions not known in advance (cf., the patterns in Figs. 10 and 11), requires the use of an experimental technique enabling the direction of the component observed to be chosen and modified after the recording is made and the hole drilled. Single beam speckle photography with spatial filtering and holographic interferometry with normal illumination and multiple viewing directions enable the in-plane and oblique components, respectively detected, to be rotated all around the *z*-axis.

Referring once again to pure in-plane components, it should be noted that, although techniques like speckle interferometry or moiré interferometry can be rendered more sensitive than

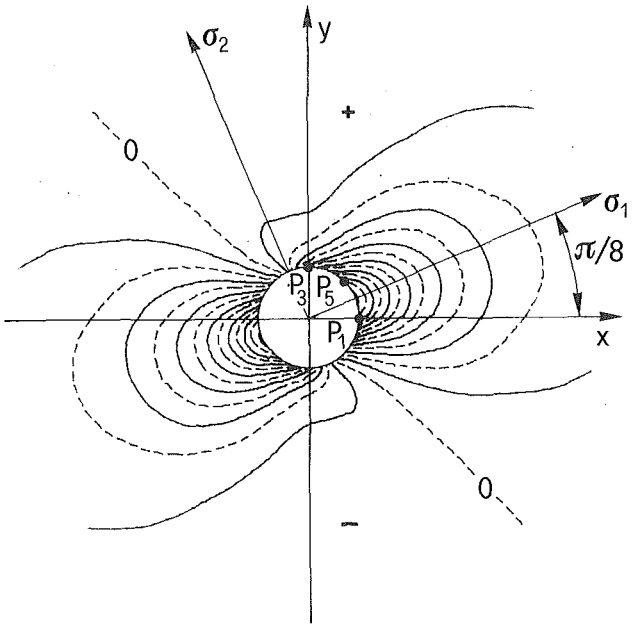

(a)

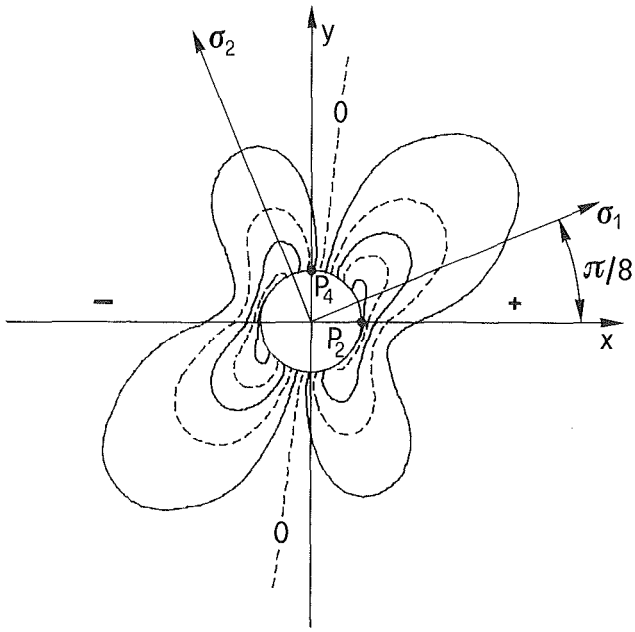

(b)

Fig. 12 In-plane displacement for a case where the x- and y-directions do not coincide with the principal axes: (a) in the x direction; (b) in the y direction

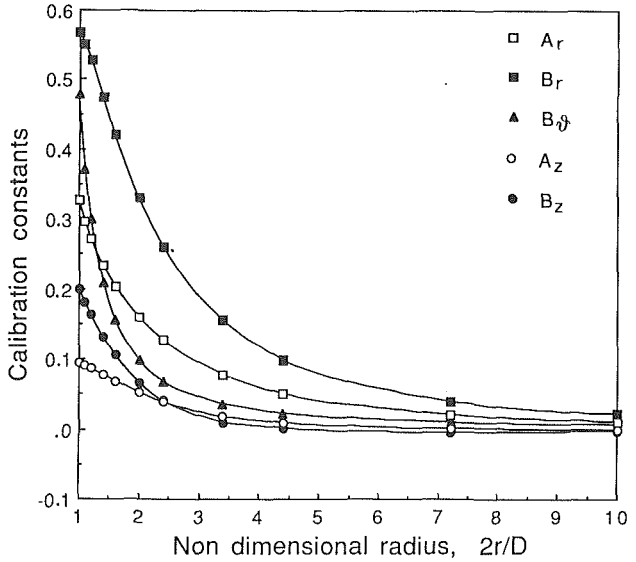

Fig. 13 Radial variation of the calibration constants for $p/D = 1$ and $\nu = 0.3$

speckle photography (i.e., $N \simeq 2$), they are only capable of detecting displacements along one direction (or even two but usually no more than three) which is defined once and for all when the optical setup is assessed or the moiré grating is attached to the specimen. Therefore, if the principal directions are not known in advance, it is obviously most improbable to obtain fringe patterns like those shown in Fig. 11; it would indeed be far more likely to observe fringe patterns similar to those reported in Fig. 12(*a*) and 12(*b*), where the principal directions no longer coincide with the directions of the displacements detected.

Interpreting these fringe patterns is somewhat more cumbersome, since three unknowns must be determined in order to resolve the state of stress. For this purpose, it is convenient to rewrite the radial and tangential components of displacement as:

$$u_r = D\left(A_r\frac{\sigma_x+\sigma_y}{\mathrm{E}} + B_r\frac{\sigma_x-\sigma_y}{\mathrm{E}}\cos 2\theta - B_r\frac{2\tau_{xy}}{\mathrm{E}}\sin 2\theta\right)$$
$$u_\theta = D\left(-B_\theta\frac{\sigma_x-\sigma_y}{\mathrm{E}}\sin 2\theta - B_\theta\frac{2\tau_{xy}}{\mathrm{E}}\cos 2\theta\right) \tag{29}$$

where the angle θ is now measured from the x axis of the coordinate system.

By substituting relations (29) into relations (22), fringe orders at points P_1 and P_3 in Fig. 12(*a*) can be written as:

$$n(P_1) = n_x(0) = N\frac{D}{\lambda}\left(A_r\frac{\sigma_x+\sigma_y}{\mathrm{E}} + B_r\frac{\sigma_x-\sigma_y}{\mathrm{E}}\right)$$
$$n(P_3) = n_x\left(\frac{\pi}{2}\right) = N\frac{D}{\lambda}\left(-B_\theta\frac{2\tau_{xy}}{\mathrm{E}}\right) \tag{30}$$

and fringe orders at points P_2 and P_4 in Fig. 12(*b*) as:

$$n(P_2) = n_y(0) = N\frac{D}{\lambda}\left(-B_\theta\frac{2\tau_{xy}}{\mathrm{E}}\right)$$
$$n(P_4) = n_y\left(\frac{\pi}{2}\right) = N\frac{D}{\lambda}\left(A_r\frac{\sigma_x+\sigma_y}{\mathrm{E}} - B_r\frac{\sigma_x-\sigma_y}{\mathrm{E}}\right) \tag{31}$$

The second of equations (30), or equivalently the first of (31), can be solved for $2\tau_{xy}$, while the first of (30) together with the second of (31) can be solved for $(\sigma_x+\sigma_y)$ and $(\sigma_x-\sigma_y)$. Equations (30) and (31) reduce obviously to equations (26) when $\tau_{xy}=0$.

Should only one fringe pattern be available, a third fringe measurement can be taken on the same pattern (say that in Fig. 12(*a*), at 45 deg). The equation giving the fringe order at point P_5

$$n(P_5) = n_y\left(\frac{\pi}{4}\right) = N\frac{D}{\lambda}\frac{\sqrt{2}}{2}\left(A_r\frac{\sigma_x+\sigma_y}{E} + B_\theta\frac{\sigma_x-\sigma_y}{E} - B_r\frac{2\tau_{xy}}{E}\right) \quad (32)$$

can, in fact, be used in conjunction with equations (30) to give a linear system of independent equations which can be solved for the three unknowns.

It could be easily shown that the above approach enables the stress field to be derived from the fringe pattern representing any component of displacement; the accuracy achieved will depend on the displacement component observed and on the orientation of the principal stresses.

For the sake of completeness, Fig. 13 shows the radial variation of the calibration constants for the test case reported ($p/D = 1$, $\nu = 0.3$). By introducing the proper values of the constants into equations (11), it is possible to calculate displacement variation along circles of any radius.

6 Conclusions

The displacement calibration constants introduced in the present paper enable a uniform residual stress field to be evaluated from any displacement component measured at the edge of a blind hole produced in the stressed body.

The classical hole-drilling technique can thus be applied in conjunction with any coherent optics technique which is capable of measuring the displacement field around the hole.

Significant test cases have been reported for the full field experimental methods most commonly employed and criteria have been suggested for interpreting the corresponding fringe patterns. Although pointwise techniques can also be applied, they have not been considered in the paper.

The approaches proposed for deriving the state of stress are particularly straightforward since they require the minimum number of fringe readings. Whenever the fractional fringe order cannot be estimated with sufficient precision, a poor accuracy is attained which can however be improved by applying best-fit procedures to multiple measurements.

It must be pointed out that reading the fringe order at the edge of the hole could prove unreliable whenever the drilling technique employed is not capable to produce a neat hole, i.e., a hole with no burr or plastic deformation in the neighboring material. The problem can however be easily circumvented by reading fringe orders at a certain distance from the border of the hole. All the procedures previously suggested for deriving the state of stress can be applied, provided proper calibration constants are employed in the calculations; charts plotting the radial variation of the constants (cf., Fig. 13) should obviously be available.

As a concluding remark, it is worth noting that the calibration constants given in the paper have been derived for a uniform stress field; unacceptable errors could therefore arise whenever the same constants are used in a case where stresses vary significantly either on the surface or through the thickness. On the other hand, full field techniques yield information on the degree of uniformity of the stress field, thus enabling the results obtained to be either confirmed or rejected. The analysis of the distortion introduced in the fringe patterns by the stress gradients might, moreover, permit evaluation of a not uniform residual stress field. In order to investigate the feasibility of this approach, the authors have undertaken an extensive program of numerical analyses.

References

1 "Determining Residual Stresses by the Hole-Drilling Strain-Gage Method," ASTM standard E837-85.

2 Schajer, G. S., "Application of Finite Element Calculations to Residual Stresses Measurements," ASME JOURNAL OF ENGINEERING MATERIALS AND TECHNOLOGY, Vol. 103, No. 2, 1981, pp. 157–163.

3 Schajer, G. S., "Measurement of Non-Uniform Residual Stresses Using the Hole-Drilling Method, Part I and Part II," ASME JOURNAL OF ENGINEERING MATERIALS AND TECHNOLOGY, Vol. 110, No. 4, 1988, pp. 338–349.

4 McDonach, A., McKelvie, J., MacKenzie, P., and Walker, C. A., "Improved Moiré Interferometry and Applications in Fracture Mechanics, Residual Stresses and Damaged Composites," *Experimental Techniques*, Vol. 7, No. 6, 1983, pp. 20–24.

5 Antonov, A. A., "Inspecting the Level of Residual Stresses in Welded Joints by Laser Interferometry," *Welding Production*, Vol. 30, No. 9, 1983, pp. 29–31.

6 Nelson, D. V., and McCrickerd, J. T., "Residual-Stress Determination Through Combined Use of Holographic Interferometry and Blind-Hole Drilling," *Experimental Mechanics*, Vol. 26, No. 4, 1986, pp. 371–378.

7 Nicoletto, G., "A Moiré Interferometric Hole-Drilling Method for the Determination of Residual Stresses," Joint SEM/BSSM International Conference on Advanced Measurement Techniques, London, 1987, pp. 24–27.

8 Furgiuele, F. M., Pagnotta, L., and Poggialini, A., "Application of Holographic Interferometry to the Hole-Drilling Technique for Determining Residual Stresses," *Proc. of the XV National Conference AIAS*, Pisa, Italy, 1987, pp. 607–620 (in Italian).

9 Luchi, M. L., and Poggialini, A., "The Application of the Boundary Element Method to the Solution of 3-Dimensional Elasticity Problems," *Proc. of the IX National Conference AIAS*, Florence, Italy, 1980, pp. 293–302 (in Italian).